

Synchrotron Polarization Signatures of Surface Waves in Supermassive Black Hole Jets

J. Davelaar^{1,2} , B. Ripperda^{3,4,5,6} , L. Sironi² , A. A. Philippov⁷ , H. Olivares⁸ , O. Porth⁹ , B. van den Berg⁸,

T. Bronzwaer⁸ , K. Chatterjee^{10,11} , and M. Liska¹²

¹ Center for Computational Astrophysics, Flatiron Institute, 162 Fifth Avenue, New York, NY 10010, USA; jdavelaar@flatironinstitute.org
² Department of Astronomy and Columbia Astrophysics Laboratory, Columbia University, 550 West 120th Street, New York, NY 10027, USA

³ Canadian Institute for Theoretical Astrophysics, 60 St. George Street, Toronto, ON M5S 3H8, Canada

⁴ Department of Physics, University of Toronto, 60 St. George Street, Toronto, ON M5S 1A7, Canada

⁵ David A. Dunlap Department of Astronomy, University of Toronto, 50 St. George Street, Toronto, ON M5S 3H4, Canada

⁶ Perimeter Institute for Theoretical Physics, 31 Caroline Street North, Waterloo, ON N2L 2Y5, Canada

⁷ Department of Physics, University of Maryland, College Park, MD, USA

⁸ Department of Astrophysics/IMAPP, Radboud University, P.O. Box 9010, 6500 GL Nijmegen, The Netherlands

⁹ Anton Pannekoek Instituut, Universiteit van Amsterdam P.O. Box 94249, 1090 GE Amsterdam, The Netherlands

¹⁰ Black Hole Initiative at Harvard University, 20 Garden Street, Cambridge, MA 02138, USA

¹¹ Harvard-Smithsonian Center for Astrophysics, 60 Garden Street, Cambridge, MA 02138, USA

¹² Institute for Theory and Computation, Harvard University, 60 Garden Street, Cambridge, MA 02138, USA

Received 2023 September 14; revised 2023 October 20; accepted 2023 October 24; published 2023 December 6

Abstract

Supermassive black holes in active galactic nuclei are known to launch relativistic jets, which are observed across the entire electromagnetic spectrum and thought to be efficient particle accelerators. Their primary radiation mechanism for radio emission is polarized synchrotron emission produced by a population of nonthermal electrons. In this Letter, we present a global general relativistic magnetohydrodynamical (GRMHD) simulation of a magnetically arrested disk (MAD). After the simulation reaches the MAD state, we show that waves are continuously launched from the vicinity of the black hole and propagate along the interface between the jet and the wind. At this interface, a steep gradient in velocity is present between the mildly relativistic wind and the highly relativistic jet. The interface is, therefore, a shear layer, and due to the shear, the waves generate roll-ups that alter the magnetic field configuration and the shear layer geometry. We then perform polarized radiation transfer calculations of our GRMHD simulation and find signatures of the waves in both total intensity and linear polarization, effectively lowering the fully resolved polarization fraction. The telltale polarization signatures of the waves could be observable by future very long baseline interferometric observations, e.g., the next-generation Event Horizon Telescope.

Unified Astronomy Thesaurus concepts: [Astrophysical black holes \(98\)](#); [Supermassive black holes \(1663\)](#); [Active galactic nuclei \(16\)](#); [Jets \(870\)](#); [Relativistic jets \(1390\)](#); [Radiative transfer simulations \(1967\)](#); [Plasma astrophysics \(1261\)](#); [Polarimetry \(1278\)](#)

1. Introduction

Accreting supermassive black holes can produce highly relativistic electromagnetically collimated outflows called jets, observed across the electromagnetic spectrum. These jets can be observed up to kiloparsec scales in the case of active galactic nuclei (AGN). At radio and millimeter frequencies, the primary emission mechanism is synchrotron emission. Very long baseline interferometric (VLBI) observations probe the jet substructure and reveal edge-brightened morphology, often referred to as limb brightening (see, e.g., Giovannini et al. 2018; Kim et al. 2018; Walker et al. 2018; Janssen et al. 2021). However, the mechanism responsible for energizing the radiating electrons along the jet surface remains an active debate. The upcoming next-generation VLBI facilities will bring a higher resolving power and dynamic range, allowing for better-resolved AGN jet images and polarization maps. In this work, we investigate the imprint of instabilities in the jet boundary and the effect of nonthermal tails in electron

distribution functions (DFs) on polarized emission features of AGN jets.

Since synchrotron emission is intrinsically linearly polarized (Rybicki & Lightman 1979), where the polarization vector is perpendicular to the magnetic field lines, the observed polarization from AGN can be used to study the magnetic field structure of jets. These systems generally show very low linear polarization (LP) fractions across the entire radio band (see, e.g., Zavala & Taylor 2003; Hada et al. 2016; Walker et al. 2018; Park et al. 2019; EHT MWL Science Working Group et al. 2021). These low fractions indicate that an external Faraday screen depolarizes the jet's emission before it reaches us or that the emission from the jet is not generated in large-scale coherent magnetic field geometries. In the case of M87 at submillimeter wavelengths, observations by Hada et al. (2016) show LP fractions of up to 20%, revealing regions of coherent field geometry when observed at higher spatial resolution.

The highest-resolution polarized observations of a low-luminosity AGN (LLAGN) to date are by the Event Horizon Telescope Collaboration et al. (2021). The Event Horizon Telescope (EHT) showed that in M87* at horizon scales, the polarization vector shows a helical pattern, which is typically reproduced by simulations of accretion flows in the magnetically arrested disk (MAD) state (Igumenshchev et al. 2003; Narayan et al. 2003; Tchekhovskoy et al. 2011). MAD



Original content from this work may be used under the terms of the [Creative Commons Attribution 4.0 licence](#). Any further distribution of this work must maintain attribution to the author(s) and the title of the work, journal citation and DOI.

accretion flows can be studied with general relativistic magnetohydrodynamical (GRMHD) simulations. To study the emission generated by the GRMHD simulations, they can be postprocessed with general relativistic radiative transfer codes (Dexter et al. 2012; Mościbrodzka et al. 2017; Davelaar et al. 2018; Wong et al. 2021; Cruz-Osorio et al. 2022; Fromm et al. 2022) after postulating an electron temperature prescription. A magnetically arrested flow typically reaches a limit where the magnetic pressure balances the gas pressure due to accumulated magnetic flux on the event horizon. This limit is often identified with $\phi_{\text{mad}} = \Phi_B / \sqrt{M} \approx 15$ (Tchekhovskoy et al. 2011), where Φ_B is the magnetic flux threading the horizon, and \dot{M} is the mass accretion rate. If this threshold is reached, the antiparallel magnetic field lines in the northern and southern jets are compressed to form a thin current sheet that reconnects and expels the magnetic flux (Dexter et al. 2020; Ripperda et al. 2020, 2022). During such magnetic flux eruptions, the magnetic field undergoes no-guide-field reconnection, resulting in the expulsion of a flux tube consisting of a vertical (poloidal) magnetic field. This flux tube can push the accretion disk away, effectively arresting a part of the incoming flow. The flux tubes can orbit at sub-Keplerian velocities in the disk, where they can propagate to a few tens of gravitational radii. Within one orbit, the low-density fluid in the flux tube gets mixed into the higher-density disk through magnetic Rayleigh–Taylor instability (RTI; Ripperda et al. 2022; Zhdankin et al. 2023). The magnetic flux eruptions are conjectured to power high-energy flares through reconnection near the horizon (Dexter et al. 2020; Ripperda et al. 2020, 2022; Hakobyan et al. 2023) and through reconnection induced by RTI at the boundary of the orbiting flux tube (Porth et al. 2021; Zhdankin et al. 2023).

In this Letter, we will use GRMHD simulations in Cartesian Kerr–Schild (CKS) coordinates with adaptive mesh refinement to study the large-scale properties of the jets. Using Cartesian coordinates in combination with adaptive mesh refinement allows us to better resolve the shear layer separating the highly relativistic bulk velocity jet and the mildly relativistic disk. We will refer to this region as the jet–wind shear layer. Our simulation shows that the magnetic flux eruptions associated with MAD flows can drive waves along the jet–wind shear layer. At larger radii, the waves show roll-ups that mix high-density wind material with the low-density magnetized jet. In this nonlinear phase, the waves may trigger magnetic reconnection and turbulence, as was found in local-box simulations (Sironi et al. 2021). To quantify the imprint of the waves on the observables, we ray-trace our simulation with our polarized radiative transfer code RAPTOR (Bronzwaer et al. 2018, 2020). We find that the waves depolarize the observed synchrotron emission.

This Letter is structured as follows. Section 2 describes our numerical setup and summarizes how we compute synthetic polarized images. Section 3 explains our GRMHD and radiative transfer results, highlights LP and circular polarization (CP) properties, and provides evidence that the existence of waves results in depolarization. Finally, in Section 4, we discuss and summarize our main conclusions.

2. Numerical Setup

In this section, we will describe our GRMHD simulation setup, radiative transfer code, and electron thermodynamics model.

2.1. GRMHD

To model the dynamics of the accretion flow around a Kerr black hole, we use the Black Hole Accretion Code (BHAC; Porth et al. 2017; Olivares et al. 2019), which solves the ideal GRMHD equations in curved spacetime. The equation of state is assumed to be an ideal gas law, described via the specific enthalpy

$$h(\rho, P_{\text{gas}}) = 1 + \frac{\gamma_{\text{ad}}}{\gamma_{\text{ad}} - 1} \frac{P_{\text{gas}}}{\rho}, \quad (1)$$

with gas pressure P_{gas} and mass density ρ in the fluid frame, and the adiabatic index is set to $\gamma_{\text{ad}} = 13/9$.

We initialize our simulation with a Fishbone & Moncrief (1976) torus in spherical Boyer–Lindquist coordinates (t, r, θ, ϕ) , where θ is the angle with respect to the spin axis of the black hole, and ϕ is the azimuthal angle around the black hole spin axis. The initial conditions are then transformed to CKS coordinates (t, x, y, z) . The initial disk has an inner radius of $r_{\text{in}} = 20r_g$, with r_g the gravitational radius given by $r_g = GM/c^2$, where G is Newton’s constant, M is the black hole mass, and c is the speed of light. We set the pressure maximum of the disk at $r_{\text{max}} = 40r_g$. The initial magnetic field is given by the vector potential $A_\phi = \rho(r/r_{\text{in}} \sin \theta)^3 e^{-r/400} - 0.2$, where r is the radial coordinate, and θ is the polar angle. The vector potential follows isocontours of density ρ . These initial conditions are chosen such that the simulation will reach the saturated state of a MAD accretion flow.

We set the dimensionless black hole spin parameter to $a = 15/16$, which results in a black hole horizon size of $r_h \approx 1.34r_g$. The domain size is $(-4000r_g, 4000r_g)$ in all three spatial Cartesian directions. Our base resolution is 192^3 cells. We employ nine additional levels of static mesh refinement, resulting in an effective uniform Cartesian resolution of $98,304^3$. The highest-resolution grid is centered at the horizon and has a resolution of $\Delta x_i = 0.08r_g$. The simulation is run for $10,000r_g/c$. We introduce a maximum for the cold magnetization parameter $\sigma = \frac{b^2}{\rho}$, where b is the magnetic field strength, and we inject mass to maintain $\sigma \leq 100$. Additionally, we ensure that $\beta_p^{-1} \leq 10^3$, where $\beta_p = 8\pi P_{\text{gas}}/b^2$ is the plasma beta parameter. We use floor profiles for density as well as pressure, given by $\rho_{\text{floor}} = 10^{-4}r^{-2}$ and $P_{\text{floor}} = 10^{-6}\rho_{\text{floor}}^{\gamma_{\text{ad}}}$. Due to our Cartesian grid, we do not have an inner radius where we can employ outflowing boundary conditions; we therefore introduce an artificial treatment of the fluid variables inside the black hole event horizon, known as excision in numerical relativity, to limit the accumulation of energy and density, which otherwise could numerically diffuse out of the event horizon when accumulated to too-high values. In our case, we introduce a ceiling on density ($\rho_{\text{max}} = 6$), as well as pressure ($P_{\text{max}} = 2$) when $r < r_{\text{crit}}$, where our critical radius is set to be $r_{\text{crit}} = 1r_g$. Given the location of the critical radius, we have four cells between the event horizon and the critical radius.

2.2. Synthetic Polarized Images

To generate synthetic polarized images of the accretion flow, we use the general relativistic ray-tracing code RAPTOR. RAPTOR solves the polarized radiative transport equations along null geodesics. The geodesic equation is solved starting from a virtual camera outside the simulation domain ($r_{\text{cam}} = 10^4r_g$). We employ an adaptive camera as described

in Davelaar & Haiman (2022). The adaptive camera allows a varying resolution over the image plane, resulting in a computational benefit, since most of the resolution can be focused on the event horizon scale, which shows small-scale emission varying on short timescales, while the larger scale can be fully resolved with a lower resolution. We use a base resolution of 625^2 pixels and double the resolution four times, within $60r_g$, $40r_g$, $20r_g$, and $10r_g$, bringing the effective resolution to $10,000^2$ pixels.¹³ We use an adaptive Runge–Kutta–Fehlberg method to integrate the geodesic equation and a fourth-order finite difference method to compute the metric derivatives needed for the Christoffel coefficients. The step size in RAPTOR is estimated based on the wavevector in the previous step; see Davelaar et al. (2019). For this work, we developed an additional step-size criterion based on a Courant–Friedrichs–Lewy condition, where we require a minimum of eight steps per cell to ensure convergence of all Stokes parameters. We compute synthetic images between 80 and 100 GHz with a frequency spacing of 3 GHz. We also compute time-averaged spectra from the image-integrated total intensity at 25 frequencies with a logarithmic spacing between 10^{10} and 10^{15} Hz.

The ideal GRMHD equations are dimensionless and do not describe the evolution and thermodynamics of electrons. To this end, we need to introduce a mass scaling and a prescription for the electron temperature. To scale our simulation to a specific black hole, we use a unit of length $\mathcal{L} = r_g$, a unit of time $\mathcal{T} = r_g/c$, and a unit of mass \mathcal{M} . The unit of mass is related to the mass accretion rate via $\dot{M} = \dot{M}_{\text{sim}} \mathcal{M}/\mathcal{T}$, where \dot{M}_{sim} is the accretion rate in simulation units. Combinations of these units are then used to scale all relevant fluid quantities. The density is scaled by $\rho_0 = \mathcal{M}/\mathcal{L}^3$, the internal energy by $u_0 = \rho_0 c^2$, and the magnetic fields by $B_0 = c\sqrt{4\pi\rho_0}$ (where B_0 is expressed in Gaussian units). Since the black hole mass is often constrained observationally, the only free parameter in our system is \mathcal{M} , which can be used to set the energy budget of the simulation such that the total emission produced equals a user-set target. We follow Mościbrodzka et al. (2016) to parameterize the ratio between electron temperature T_e and proton temperature T_p via

$$T_{\text{ratio}} = \frac{1}{1 + \beta_p^2} + R \frac{\beta_p^2}{1 + \beta_p^2},$$

$$\Theta_e = k_b T_e / m_e c^2 = \frac{U(\gamma_{\text{ad}} - 1)m_p/m_e}{\rho(1 + T_{\text{ratio}})}, \quad (2)$$

where U is the internal energy, m_p is the proton mass, m_e is the electron mass, and Θ_e is the dimensionless electron temperature. The variable R is a free parameter that sets the temperature ratio in regions where $\beta_p \gg 1$, allowing for different emission morphology depending on the choice of R , e.g., disk-dominated if $R = 1$ or jet-dominated if $R \gg 1$. Here, we will limit ourselves to $R = 20$, e.g., a more jet-dominated model. Note that MADs are relatively insensitive to the exact value of R given that most of the emission originates from a region where $\beta_p \lesssim 1$. Finally, we must choose the electron DF's shape and spatial variation. We consider two models, one

¹³ This significantly reduces the computation cost, since the effective resolution uses a factor of 50 fewer pixels compared to a standard uniform camera.

where the DF is limited to a thermal relativistic Maxwell–Jüttner DF (MJ-DF), and one where we combine the MJ-DF with a κ -DF. The κ -DF deviates from an MJ-DF by having a thermal core and a power law at high Lorentz factors. The κ -DF (Xiao 2006) is given by

$$\frac{dn_e}{d\gamma} = n_e N \gamma \sqrt{\gamma^2 - 1} \left(1 + \frac{\gamma - 1}{\kappa w}\right)^{-(\kappa+1)}, \quad (3)$$

where the free parameters are w , which sets the width of the distribution, and κ , which sets the slope of the power law, and N is a normalization constant such that $\int_1^\infty \frac{dn_e}{d\gamma} d\gamma = n_e$. The κ parameter is related to the power-law index p of the nonthermal tail of the DF via $\kappa = p + 1$, such that for $\gamma \gg 1$, $\frac{dn_e}{d\gamma} \propto \gamma^{1-\kappa}$. For the width w , we follow Davelaar et al. (2019) by enforcing that the energy in the DF equals the total available internal energy of the electrons,

$$w = \frac{(\kappa - 3)}{\kappa} \Theta_e, \quad (4)$$

where Θ_e is computed with Equation (2). Note that this formula requires $\kappa > 3$ ($p > 2$).

We then compute the emission coefficients c_ν (emission, absorption, and rotation coefficients) using a prescription introduced in Event Horizon Telescope Collaboration et al. (2022) that combines thermal and κ coefficients via

$$c_\nu = (1 - \eta(\beta_p, \sigma)) c_{\text{thermal}} + \eta(\beta_p, \sigma) c_\kappa, \quad (5)$$

$$\eta(\beta_p, \sigma) = (1 - e^{-\beta_p^{-2}})(1 - e^{-(\sigma/\sigma_0)^2}), \quad (6)$$

where σ_0 sets the transition point for the magnetization, which we set to $\sigma_0 = 0.5$. The function $\eta(\beta_p, \sigma)$ smoothly transitions from thermal to nonthermal components if $\beta_p < 1$ and $\sigma/\sigma_0 > 1$, representing sites with a large reservoir of magnetic energy that can dissipate to accelerate particles, e.g., in the jet's shear layer. The polarized radiation transfer coefficients are computed via a fit formula. For the thermal DF, we use the emission and absorption coefficients presented in Dexter (2016) and the rotativities from Shcherbakov (2008); for the κ -DF, we follow Pandya et al. (2016) and Marszewski et al. (2021).

As an archetype LLAGN, we use model parameters consistent with M87*, meaning a black hole mass of $M = 6.5 \times 10^9 M_\odot$ and a distance of $d = 16.8$ Mpc (Event Horizon Telescope Collaboration et al. 2019a). We set the angle between the BH spin axis and the observer to $i = 160^\circ$, following Walker et al. (2018). We set \mathcal{M} such that the average flux at 86 GHz is $F_{86\text{GHz}} = 1$ Jy, as observed by EHT MWL Science Working Group et al. (2021). The spectrum obtained by EHT MWL Science Working Group et al. (2021) also shows a spectral slope in the optically thin part of the spectrum in the near-infrared (NIR) of $F_\nu \propto \nu^{-1}$. Given that for optically thin synchrotron emission, the flux follows $F \propto \nu^{-(p-1)/2} = \nu^{-(\kappa-2)/2}$, to match the observed spectral slope in the NIR, we need to use $\kappa = 4$.

To exclude the emission from the spine (interior of the jet, which in GRMHD simulations is typically dominated by artificial density floors), we exclude all of the emission if $\sigma > 5$. We expect our results to be insensitive to this choice for larger σ values. However, lower σ values would result in a smaller emission region at the jet–wind interface. We also exclude the larger-scale disk, $\sqrt{x^2 + y^2} > 150r_g$, which has not settled into a steady state for the runtime of our simulation. However,

given the viewing angle of $i = 160^\circ$, this choice does not strongly affect our results.

3. Results

In this section, we summarize our results. In Section 3.1, we find that surface waves are continuously present along the jet-wind shear layer after our simulation reaches the MAD state. In Section 3.2, we fit our GRMHD model to the spectrum of M87 and show that the κ -jet model recovers the low-frequency radio and the NIR. In Section 3.3, we show synthetic maps of Stokes I that contain wavelike radially outflowing substructures that enhance the emission. In Section 3.4, we show that the magnetic flux eruptions and waves imprint themselves in various LP quantities, serving as potential telltale signatures that could be used to test M87’s putative MAD accretion flow state. In Section 3.5, we highlight that CP plays a minor role. However, we see sign reversals in CP maps that could indicate magnetic field reversals caused by the surface waves. We measure the Faraday rotation measure (RM) of our models in Section 3.6. Lastly, in Section 3.7, we provide evidence that the polarization signatures are connected to the waves seen in the GRMHD simulation.

3.1. GRMHD

To assess when the simulation reaches the MAD state, we compute at the black hole’s event horizon the mass accretion rate, \dot{m} , and magnetic flux threading the horizon, Φ_B , both in dimensionless units. The mass accretion rate is defined as $\dot{m} = \int_{r=r_h} \rho u^r \sqrt{g} d\theta d\phi$, where u^r is the radial component of the velocity, and \sqrt{g} is the determinant of the metric. The magnetic flux is defined as $\Phi_B = 0.5 \int_{r=r_h} |B^r| \sqrt{\gamma} d\theta d\phi$, where B^r is the radial component of the magnetic field, and $\sqrt{\gamma}$ is the determinant of the spatial part of the metric.¹⁴ We also define the MAD parameter $\phi_{\text{mad}} = \Phi_B / \sqrt{\dot{m}}$, which was introduced by Tchekhovskoy et al. (2011) to quantify that a simulation reaches the MAD state when $\phi_{\text{mad}} \sim 15$. All three quantities, \dot{m} , Φ_B , and ϕ_{mad} , are shown in Figure 1. The accretion flow reaches the MAD state for the first time at $\approx 3000r_g/c$, when the magnetic flux on the horizon saturates as $\phi_{\text{mad}} \sim 15$. Our MAD simulation shows globally similar properties to standard simulations on spherical grids; see Appendix A for a comparison.

In Figure 2, we show two-dimensional maps of the logarithm of density sliced along the spin axis (top row) or the equatorial plane (bottom row). Initially, the jet is more laminar in the left column, as flux is still building up on the horizon, and no eruptions have occurred. In the middle column, after the system has reached the MAD limit, flux tubes can be seen in the x -plane, indicated by lower densities in the disk. The exhaust from magnetic flux eruptions generates these flux tubes. During the eruptions, magnetic energy is dissipated via large equatorial current sheets generated when the disk becomes magnetically arrested, and the northern and southern jets get in direct contact (Ripperda et al. 2022). The exhaust of these sheets forms flux tubes containing vertical magnetic fields that spiral outward in the disk before dissipating due to Rayleigh–Taylor mixing (Zhdankin et al. 2023).

¹⁴ Note that we use the spatial part of the metric here, which differs from the mass accretion, since BHAC uses $3 + 1$ formalism, which results in the lapse function being contracted in the definition of the magnetic fields.

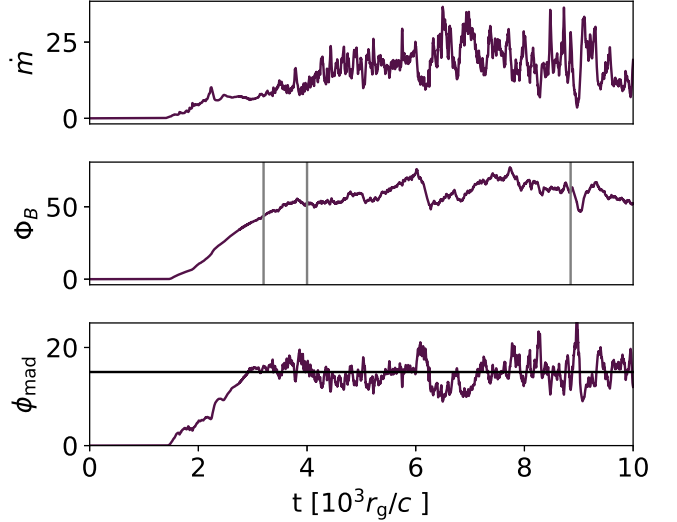


Figure 1. Time series in dimensionless units of horizon-integrated mass accretion rate \dot{m} (top panel), magnetic flux Φ_B (middle panel; gray lines correspond to the slices shown in Figure 2), and the MAD parameter $\phi_{\text{mad}} = \Phi_B / \sqrt{\dot{m}}$ (bottom panel). The MAD parameter saturates at $\phi_{\text{mad}} \approx 15$, corresponding to the horizontal black line.

In the middle panel, small-amplitude waves propagate along the shear layer, interfacing the higher-density disk wind and low-density jet in the top panel. Large-amplitude waves propagate outward in the right column because the system produces strong magnetic flux eruptions; see Figure 1 at $t = 8800r_g/c$. The panels correspond to the vertical lines in the middle panel of Figure 1. The variability introduced by the flux eruptions at the base of the jet acts like a forced oscillator, introducing waves that propagate and grow from near the event horizon to the shear layer between the jet and the disk. The waves propagate to large scales, growing in size while shearing magnetic field lines and generating field reversals, shown in Figure 3.

To assess the potential effect of the waves on the polarized emission, we show slices along the x - z plane in Figure 4 at $t = 8850r_g/c$ (right panels of Figure 2) of several quantities relevant to the radiation transport. We find that distinct patches of magnetization close to $\sigma \sim 1$ can be seen along the jet-wind shear layer coinciding with the location of the waves in the top right panel of Figure 2. The higher magnetization is important, since particle acceleration is more efficient at higher magnetization values (Sironi & Spitkovsky 2014). We use a passively advected tracer to study the acceleration of wind-based material to relativistic speeds at the jet-wind surface. The tracer is set to 0 when the density or pressure is set to floors and set to 1 in the initial torus. We then evolve this quantity as a passive scalar, tracing the advection of disk-based material into regions that were at least once set to floors. We find that matter from the disk (unfloored material) around the location of the jet-wind shear layer waves is accelerated to a high bulk Lorentz factor, and emission generated in the waves is emitted from unfloored matter originating from the accretion disk, shown by a nonzero tracer and $\Gamma \geq 2$ in the top right panel of Figure 4. Looking at the bottom left panel, the waves also correlate with regions with a large fraction of nonthermal electrons since $\eta \sim 1$, which is an evident result of the high magnetization (and low plasma- β) and our choice of electron distribution model (Equation (6)). Finally, the electrons are relativistically hot (i.e., $\Theta_e > 1$), as shown in the bottom right panel. We associate the relativistic

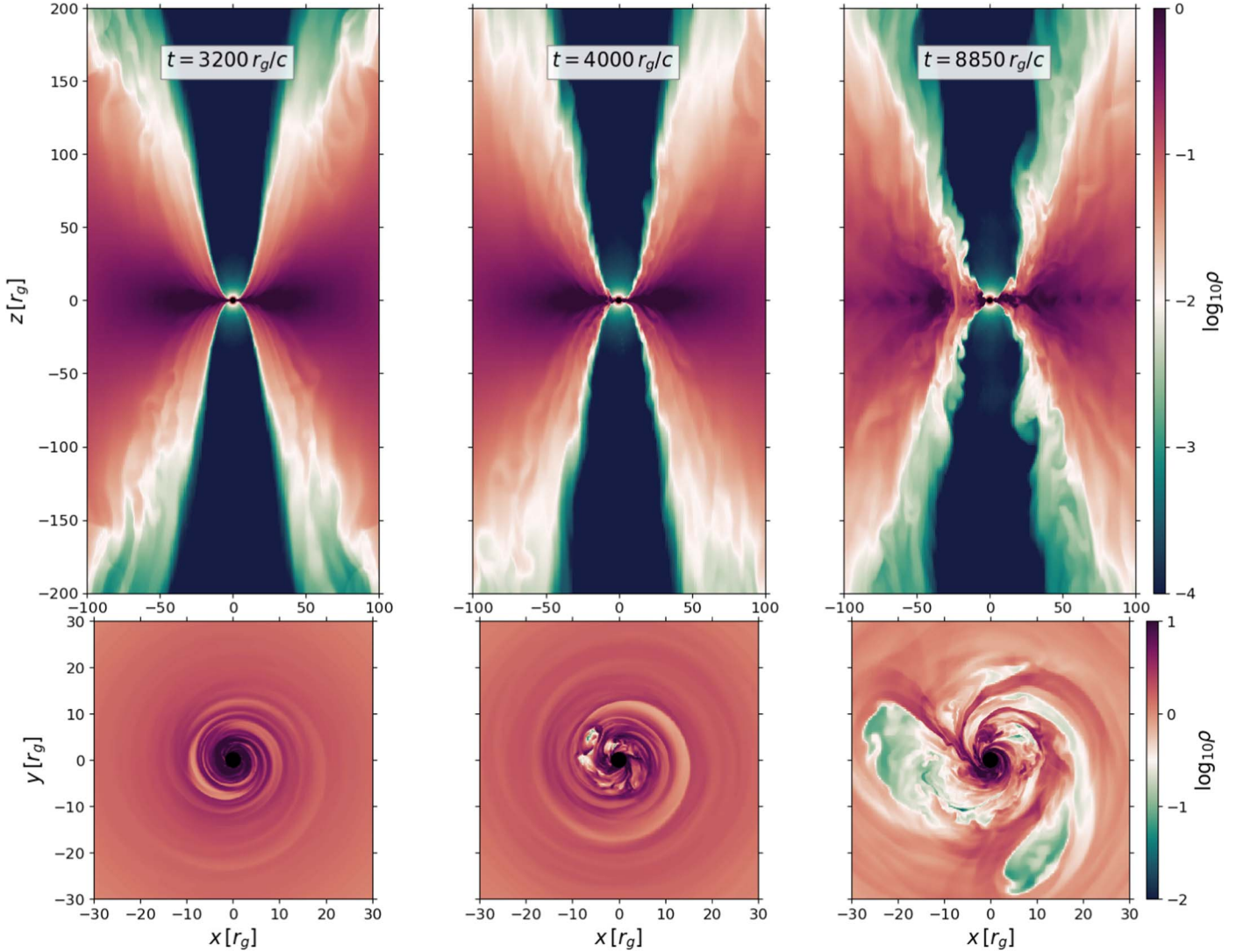


Figure 2. Density profiles in the x - z plane (top row) and x - y plane (bottom row; notice the different axis scaling compared to the top row). The left column shows the simulation at $t = 3200r_g/c$, well before the magnetic flux is saturated and a MAD state is reached. At this point, the jet-wind shear layer is more laminar. Middle column: at $t = 4000r_g/c$, the accretion flow reaches the MAD state for the first time. In the bottom panel, small underdensity regions are visible, indicative of potential flux eruptions, which can be seen as drops in the integrated Φ_B time series shown in Figure 1. A first sign of waves can be seen in the jet-wind shear layer. Right column: simulation snapshot at $t = 8850r_g/c$. Large underdensities in the bottom panel are seen near the horizon, making the accretion flow nonaxisymmetric. The underdensities correlate with large dissipation events of Φ_B ; see again the middle panel of Figure 1. Additionally, large-scale waves are present in the jet-wind shear layer.

temperatures and the large fraction of nonthermal electrons with the heating of the plasma by the waves due to the dissipation of magnetic energy, as predicted in Sironi et al. (2021). In summary, the shear layer that is at the surface of the jet interfacing with the wind has a magnetization of order unity, has a high relativistic electron temperature, is moving at relativistic bulk Lorentz factors ($\Gamma \sim 3$), and is likely dominated by nonthermal electrons.

3.2. Spectral DFs

In Figure 5, we show the spectral DFs of our thermal-DF (thermal-jet) and κ -DF (κ -jet) models. The top panel shows the total intensity (Stokes I) as a function of frequency. The thermal-jet model recovers the low-frequency part of the spectrum accurately, e.g., $\nu < 10^{12}$ GHz; however, at higher frequencies, it drops off too fast, which is consistent with Davelaar et al. (2019). In the case of the κ -jet model, the high-

frequency emission is enhanced and obtains a spectral slope of $\alpha \approx -1$, consistent with the observations. In contrast, the thermal-jet model underestimates the NIR flux. The κ -jet model predicts that nonthermal electrons emit energetic photons predominantly in the jet boundary and are, therefore, a probe of dissipation of magnetic energy due to wave dynamics. To match the observed flux at 86 GHz, $F_{86\text{GHz}} = 1\text{Jy}$, we set the mass scaling to $\mathcal{M} = 1.5 \times 10^{25}\text{ g}$ for both the thermal and κ -jet models. These units of mass correspond to a mass accretion rate of $\approx 10^{-4}M_\odot \text{ yr}^{-1}$ and a jet power of $\approx 10^{42-43} \text{ erg s}^{-1}$, both similar to values obtained in previous works (Collaboration et al. 2019b; Chael et al. 2019; Cruz-Osorio et al. 2022) and consistent with the jet powers inferred from observations of M87 (Prieto et al. 2016).

The two bottom panels show LP and CP. For LP, the thermal jet achieves similar fluxes as the κ jet at a lower frequency ($\nu \lesssim 10^{13}$ Hz), while at a higher frequency, a clear power law is visible in the κ -jet case. A similar power law is visible for CP,

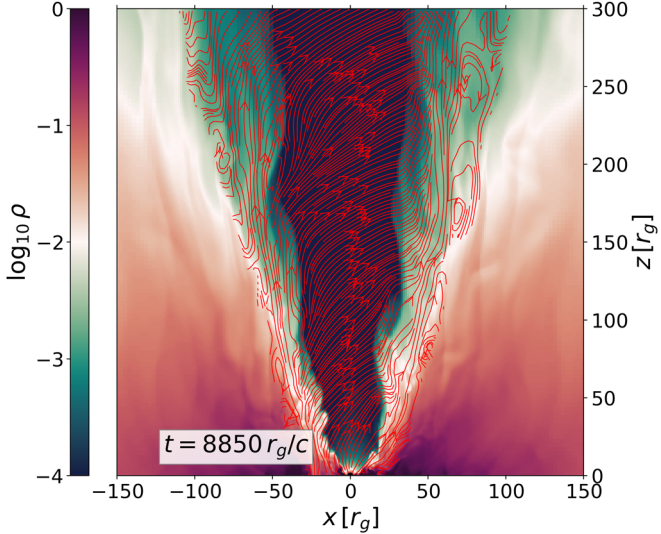


Figure 3. The density profile in the x - z plane overplotted with the magnetic field lines in the same plane. The magnetic field lines are sheared in the jet-wind shear layer, and roll-ups and magnetic islands are visible.

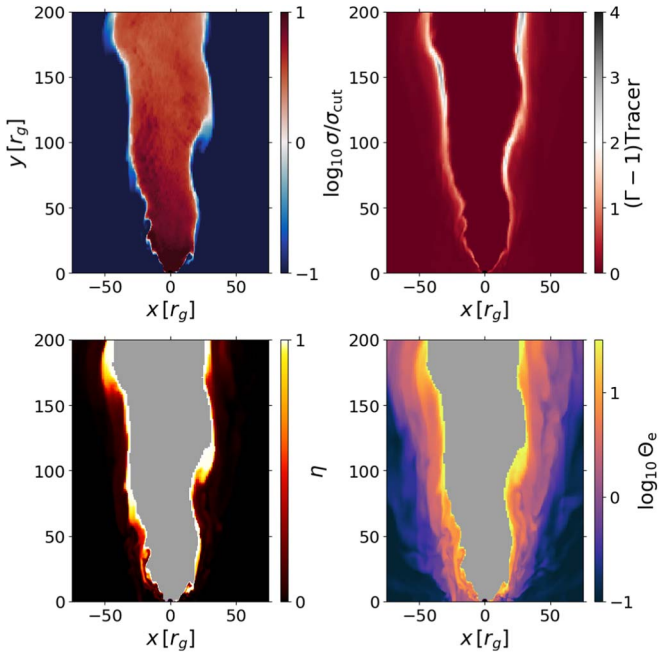


Figure 4. Simulation snapshot at the $t = 8850 r_g/c$ slice along the x - z plane of various quantities used for the radiative transfer calculation. Top left: cold magnetization $\sigma = b^2/\rho$. The inner core of the jet, which is at $\sigma \gtrsim \sigma_{\text{cut}} = 5$, is dominated by the simulation floors, also visible in Figure 2 by the low-density regions in the jet. Top right: the specific kinetic energy $\Gamma - 1$ multiplied by our passive scalar. The scalar is set to 0 for the floors and unity for disk matter. At the jet-wind shear layer, we see an increase in $\Gamma - 1$ around the locations of the waves, indicating that matter originating from the disk is mixed in the shear layer and accelerated to a high bulk Lorentz factor. Bottom left: acceleration efficiency η , where $\eta = 1$ means κ -DF only, whereas $\eta = 0$ is thermal-DF only. The jet-wind shear layer shows $\eta = 1$, coinciding with the high temperatures in the bottom right panel. The gray region indicates $\sigma \geq 5$, which is excluded from our GRRT computations. Bottom right: the electron temperature Θ_e as prescribed by Equation (1). The largest temperatures are found in the jet-wind shear layer. The gray region indicates $\sigma > 5$.

but at a lower frequency, the κ -jet model is comparable to the thermal case. Subsequent analysis is done at 86 GHz. This frequency was chosen because it probes emission structures at the base of the jet (Hada et al. 2016; Walker et al. 2018).

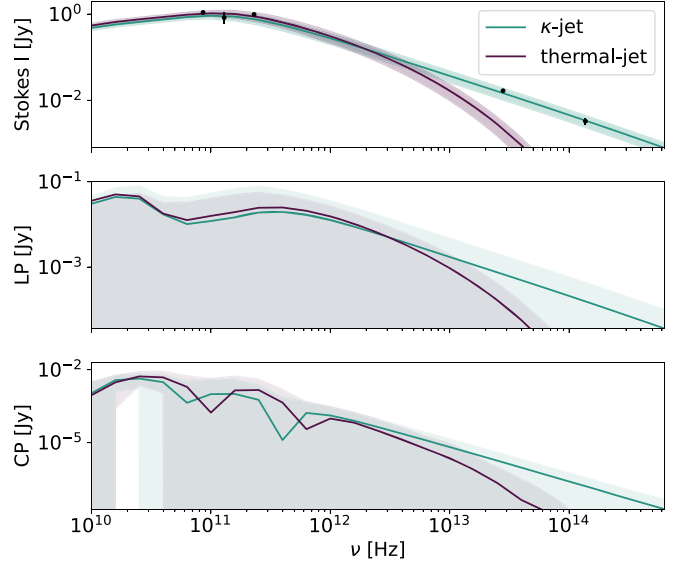


Figure 5. Spectra of time-averaged Stokes I (top panel), LP flux (middle panel), and CP flux (bottom panel) for both the κ -jet (cyan) and thermal-jet (purple) models. The shaded area shows a standard deviation on the time-averaged fluxes. The thermal jet underproduces the NIR emission compared to observations for Stokes I , while the κ jet recovers the observed spectral slope. The κ -jet model obtains similar LP and CP as the thermal jet at lower frequencies ($\nu \lesssim 10^{13}$ Hz), while at higher frequencies, it produces higher fluxes.

3.3. Total Intensity

In the first row of Figure 6, we show total intensity maps for our κ -jet model at 86 GHz. The images correspond to $t = 8500 r_g/c$ and $9300 r_g/c$. At the core of the image, a darkening is visible, corresponding to the “black hole shadow” (Luminet 1979; Falcke et al. 2000) recently observed at 86 GHz by Lu et al. (2023). At the later stage (right panel), when the surface waves are prominently visible in the GRMHD simulations, helical wavelike substructures can be distinguished within the jet at larger scales.

3.4. Linear Polarization

This subsection summarizes the LP results computed at 86 GHz. In unresolved LP fractions, we find that enhanced emission regions generate loops in a Stokes $Q - U$ diagram during the magnetic flux eruptions. The resolved LP fraction is then inversely proportional to the magnetic flux on the horizon, resulting in an enhancement of the fraction as the flux goes down. Furthermore, we find that the waves seen in the GRMHD simulation imprint themselves in LP maps as they lower the LP fraction. The effect of nonthermal κ -DF on the LP is minor, although we see a slight decrease compared to the thermal model for the LP fraction in the jet.

3.4.1. Core

In Figure 7 (top panel), we show a time series of the unresolved LP fraction m_{net} for both the thermal-jet (red lines) and κ -jet (blue lines) models, defined as

$$m_{\text{net}} = \frac{\sqrt{(\sum_{\text{pixels}} S_Q)^2 + (\sum_{\text{pixels}} S_U)^2}}{\sum_{\text{pixels}} S_I}. \quad (7)$$

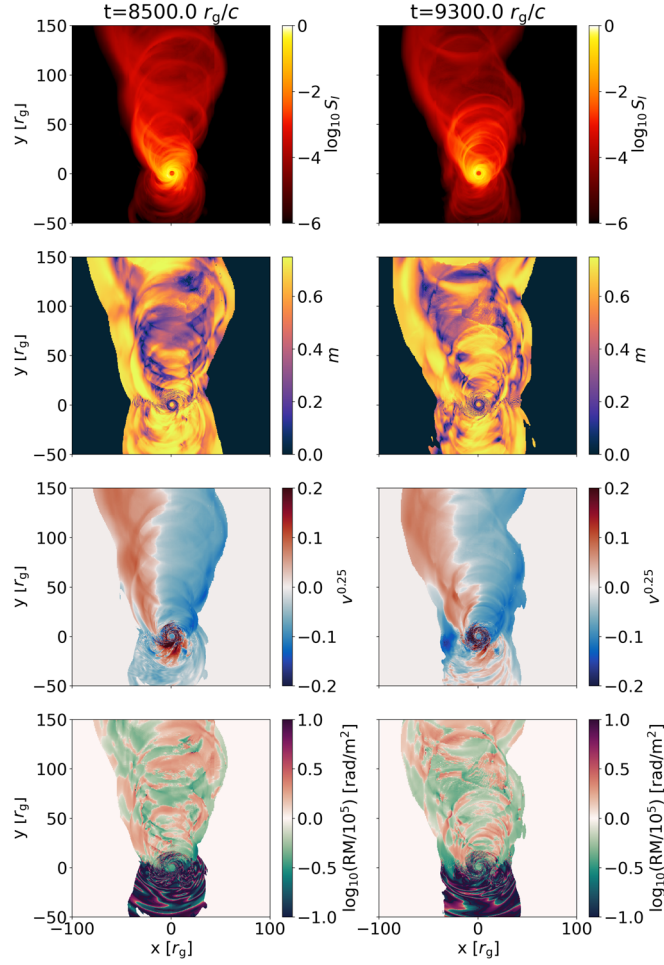


Figure 6. Synthetic synchrotron images at 86 GHz of two GRMHD simulation snapshots at $t = 8500r_g/c$ and $9000r_g/c$. First row: total intensity. Second row: LP fraction m , Equation (8). Third row: CP fraction v , Equation (9). Fourth row: RM, Equation (11), normalized by 10^5 rad m^{-2} . Large values of LP at the edges of the jet are artificial, since they are caused by regions of very low total intensity.

The image-integrated net LP fraction does not depend on telescope beam size, since it is an incoherent addition of the Stokes parameters. We obtain an average value of $m_{\text{net}} = 0.026$, consistent with the low values found by observations (Hada et al. 2016; Walker et al. 2018). The thermal and κ -jet models show almost identical values.

In Figure 7 (bottom panel), we show the resolved LP fraction, m , defined as

$$m = \frac{\sum_{\text{pixels}} \sqrt{S_Q^2 + S_U^2}}{\sum_{\text{pixels}} S_I}. \quad (8)$$

Here we follow the definition of resolved LP fraction from Equation (8) of Event Horizon Telescope Collaboration et al. (2021), which is an image-averaged LP fraction, taking into account some telescope beam size. As a first step, we assumed that the telescope fully resolves the image, taking the beam size to be much smaller than the intrinsic features we are interested in. Due to the coherent addition, the resulting resolved LP fraction m is substantially higher than the unresolved LP fraction m_{net} . The reason for this is that we preserve the sign of Q and U in the summation in the case of m_{net} , but the sign is dropped for m . In reality, Q and U will be convolved with the

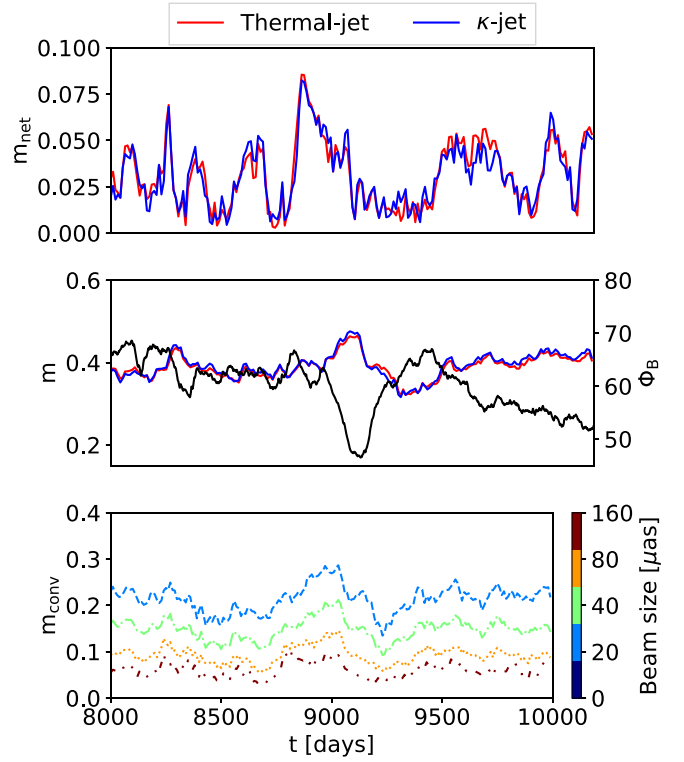


Figure 7. LP fraction as a function of time. Top panel: net LP fraction m_{net} for the thermal and κ -jet models, showing an average $m_{\text{net}} \sim 0.026$. Middle panel: resolved LP fraction m , overplotted with the magnetic flux on the horizon Φ_B (black curve). Both models show a substantially higher resolved LP fraction. Additionally, at the moment of a magnetic flux eruption, $t = 9000r_g/c$, an increase in m is visible. Bottom panel: LP fraction as a function of telescope beam size. The LP fraction decreases with increasing telescope beam size due to incoherent addition.

telescope's beam, resulting in incoherent addition. This effect can be seen in the bottom panel of Figure 7, where we compute the convolved LP fraction m_{conv} for varying telescope beam sizes of 20, 40, 80, and 160 μas . This computation is done by blurring the original images with a Gaussian filter where the full-width at half maximum represents the beam size. As the telescope beam size increases, the underlying substructure in both Q and U is being averaged out, resulting in an overall drop in LP fraction asymptotically approaching m_{net} as the beam becomes comparable to the core size.

In the fully resolved LP fraction m , as well as the 20–80 μas m_{conv} cases in Figure 7, at $t = 9000r_g/c$, an increase in LP fraction is visible. This increase coincides with a flux eruption at the horizon, visible from the overplotted Φ_B curve (solid black line, identical to the middle panel of Figure 1). The m shows a fractional increase of 20%, while Φ_B shows a fractional decrease of 20%, indicating an inverse relationship between the two quantities. A similar correlation can also be seen at the smaller eruption at $t = 8400r_g/c$. The κ -jet model reaches identical LP fractions as the thermal jet.

Close to the flux eruption starting around $t \sim 8700r_g/c$, we show the unresolved Stokes parameters in a $Q/I - U/I$ diagram. After the onset of flux eruption, we see a clear clockwise loop with an LP excess of $m_{\text{net}} \sim 0.06$ (Figure 8). The loop we find is similar to the loops found by Marrone et al. (2008) and Wielgus et al. (2022) at 230 GHz during X-ray flares for Sagittarius A*. Najafi-Ziyazi et al. (2023) finds evidence that these loops could be generated by enhanced

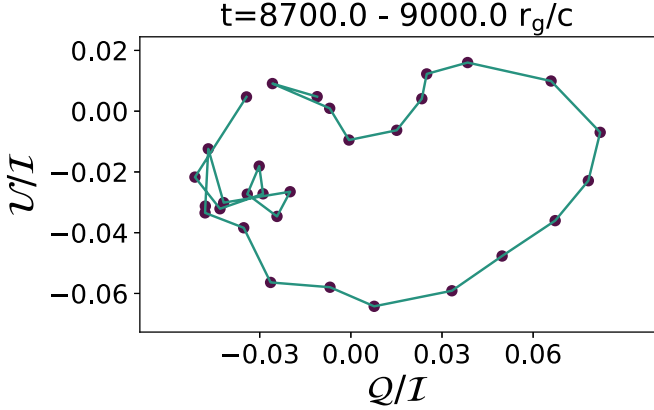


Figure 8. $Q - U$ diagram at 86 GHz. At the strongest magnetic flux eruption during the duration of our simulation at $t \sim 9000r_g/c$, we observe a pattern that manifests as a loop moving in a clockwise motion in a $Q - U$ diagram with an LP excess of $m_{\text{net}} \sim 0.06$.

polarized emission in the accretion disk by orbiting flux bundles ejected into the disk after a flux eruption. The enhanced emission leads to a local polarization excess; as the emission increases, the polarized emission increases. This enhanced emission region, often called a hot spot, orbits through the local magnetic field. Since the spot only lights up a small region of the accretion disk, it acts as a probe for the underlying magnetic field geometry. The magnetic field geometry close to the jet base is mostly poloidal; therefore, Stokes Q and U generate four quadrants, like a spoke wheel pattern, in the image plane, which alternate in sign; see, e.g., Narayan et al. (2021) and The GRAVITY Collaboration et al. (2023). Since the magnetic field orientation periodically varies, Stokes Q and U will show sinusoidal behavior in the total integrated Q and U , since an excess of either positive or negative Q and U is seen; for more details, see Vos et al. (2022) and Najafi-Ziyazi et al. (2023).

3.4.2. Jet

To study the large-scale jet only, we exclude the image plane's inner $30r_g$; in other words, we exclude the near-horizon emission. The resulting m_{net} and m are shown in Figure 9. The unresolved LP fraction m_{net} ranges from 5% to 20%. The resolved fraction, m , reaches values of around 50%. The κ -jet model shows slightly lower values than the thermal-jet model in the case of m . In the second row of Figure 6, we show a map of m . In these maps, alternating regions of high and low LP are visible, coinciding with enhanced emission in the total intensity panels in the first row. This indicates a potential correlation between the LP fraction and the presence of the waves seen in the GRMHD simulation. This potential correlation will be investigated further in Section 3.8. The LP substructure seen in our simulation in Cartesian coordinates is absent in a low-resolution MAD simulation in spherical coordinates at an effective resolution of $192 \times 96 \times 96$ cells in r , θ , and ϕ , respectively; see Appendix B.

The jet stands out as a high-intensity emission region, while the accretion disk does not contribute to the emission at larger scales ($r > 30r_g$). Comparing the total intensity map with the LP fraction map, the foreground disk surrounding the jet shows high values of m (close to unity). To understand this behavior, we evaluate the asymptotic limit of our fitting formula for the

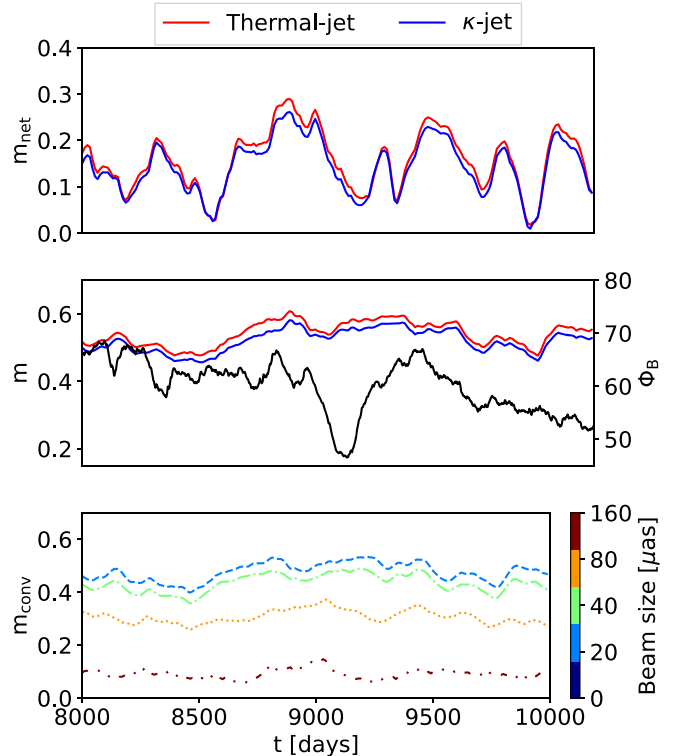


Figure 9. Identical to Figure 7 but now with the inner $30r_g$ excised from the image plane of m_{net} , m , and m_{conv} to compute the jet contribution only. Also, for the excised LP fraction, both models obtain similar fractions.

emission coefficients J_S (with S indicating one of the Stokes parameters; see Equation (31) in Pandya et al. 2016). Given that the disk has weak magnetic fields and low temperatures, we have $\nu/\nu_c \ll 1$, with $\nu_c = eB/(2\pi m_e c^2)$, and $\Theta_e \ll 1$, and we find that $J_I/|J_Q| \rightarrow 1.0$. This makes physical sense because, due to the low temperature, the thermal DF is narrow, which means that there is a quasi-monoenergetic population of electrons that is causing the emission, so the polarization fraction should go to unity. This, however, does not alter the computation of our image-integrated m , m_{conv} , and m_{net} , since this outer region has low intensity, both polarized and Stokes I , so they do not contribute to the numerator and denominator of Equations (7) and (8). Additionally, we also exclude regions of very low intensity from our map, where we set the Stokes parameters of a pixel to 0 if $S_I/\max(S_I) < 10^{-6}$.

Lastly, we compute polarization angle maps as a function of beamwidth. These can be seen in Figure 10, where we overplotted ticks of the polarization vector on top of the total intensity map from the top left panel of Figure 6. The length of the ticks is set by the LP fraction, while the angle is set by the electric vector position angle (EVPA), as defined by $\chi = \frac{1}{2} \tan^{-1}(S_Q/S_U)$; here we also exclude LP fractions when $S_I/\max(S_I) < 10^{-6}$, so the tick lengths are set to 0. For the case of zero beam size, the polarization vector clearly follows the ridges of enhanced intensity. As the beam size increases, the correlation becomes weaker. However, reorientation of the polarization vector is also visible here; e.g., at $x \sim 0r_g$ and $y \sim 50r_g$, the polarization pattern switches from diagonal, to horizontal, and back to diagonal. We only show beam sizes up to 60 μas , which is the expected resolution of the next-generation EHT (ng-EHT) at 86 GHz (Issaoun et al. 2023),

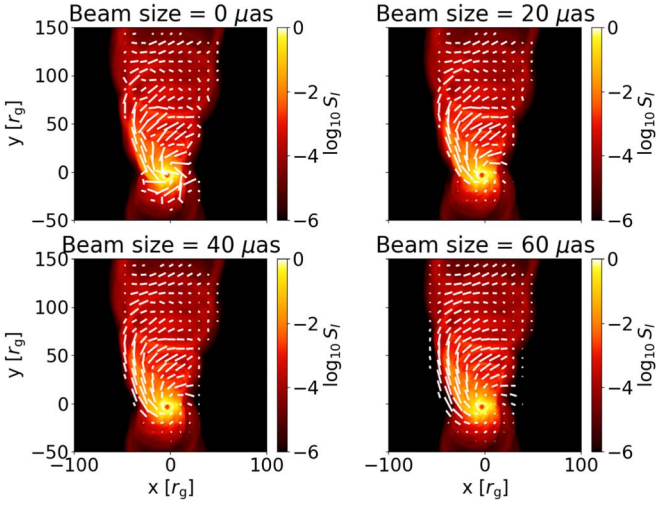


Figure 10. Polarization angle maps as a function of beam size, overplotted on the total intensity map of the top left panel of Figure 6. Top left: zero beam size. The polarization vector shows a clear correlation with the ridges seen in total intensity. For increasing beam size, this correlation becomes weaker. However, some reorientation of the vector is still visible; see, e.g., $x \sim 50r_g$, $y \sim 50r_g$.

assuming identical baselines to the current EHT array (using $\theta \sim 20 \mu\text{as}$ ($\lambda/1\text{mm}$) with $\lambda = 3 \text{ mm}$).

3.5. Circular Polarization

In this subsection, we study the CP fractions computed at 86 GHz. We find that the resolved CP fraction decreases during a flux eruption as the inner accretion disk is ejected, resulting in a more dilute plasma to perform Faraday conversion. Overall, we find low unresolved and resolved CP fractions for our thermal and κ -jet models. The CP maps show sign reversals, indicative of an alternating magnetic field orientation that coincides with the features seen in the LP maps.

3.5.1. Core

In Figure 11, we show the unresolved and resolved CP fractions, v_{net} and v , defined as

$$v_{\text{net}} = \frac{\sqrt{\left(\sum_{\text{pixels}} S_V\right)^2}}{\sum_{\text{pixels}} S_I}, \quad (9)$$

$$v = \frac{\sum_{\text{pixels}} \sqrt{S_V^2}}{\sum_{\text{pixels}} S_I}. \quad (10)$$

Both v_{net} and v are small in value, as expected from synchrotron radiation (Rybicki & Lightman 1979). In Figure 11 (bottom panel), during the strongest flux eruption at $t = 9000r_g/c$, both models show a slight decrease in CP fraction. The accretion disk enhances the amount of CP emission as Faraday conversion converts LP to CP. Due to the ejection of the inner part of the accretion disk during a flux eruption, there is more dilute plasma in this region, resulting in a drop in the CP fraction.

3.5.2. Jet

In Figure 12, we compute v_{net} and v but now also exclude the inner $30r_g$ to exclude the near-horizon emission and focus on the larger-scale jet only. This exclusion results in smaller

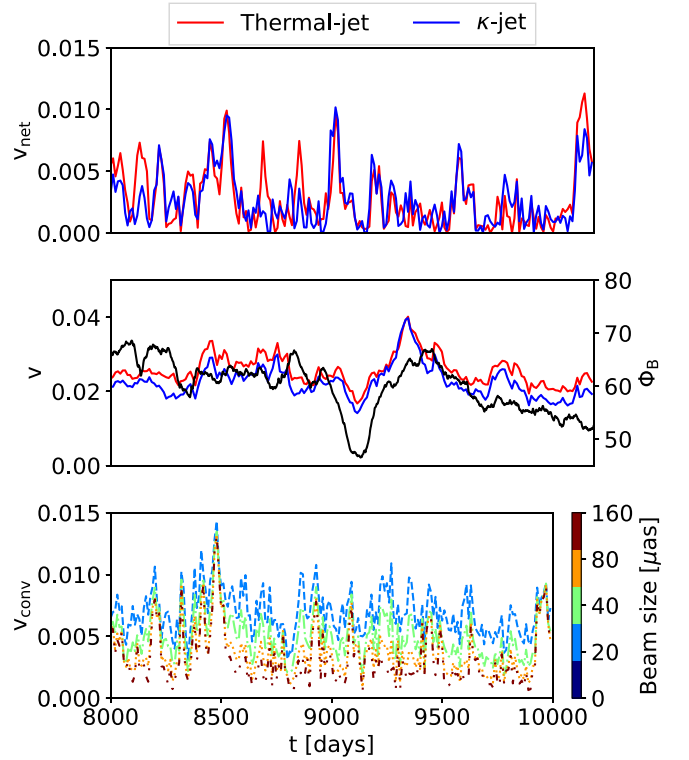


Figure 11. CP fraction as a function of time. Top panel: net CP fraction v_{net} for the thermal and κ -jet models, showing an average $v_{\text{net}} \sim 0.026$. Middle panel: resolved CP fraction v , overplotted with the magnetic flux on the horizon Φ_B (black curve). The thermal-jet and κ -jet models obtain similar CP fractions. Additionally, at the moment of a magnetic flux eruption, $t = 9000r_g/c$, a decrease in v is visible. Bottom panel: CP fraction as a function of telescope beam size. The CP fraction decreases with increasing beam size due to incoherent addition.

fractions than the entire image-integrated values, since Faraday conversion happens in high-density regions. The third row of Figure 6 shows maps of v where the CP fraction is smaller at larger radii. In the map, we preserve the sign of Stokes V , which is set by the direction of the magnetic field along the line of sight. The image shows reversals in the sign of v and additional ridges of low CP fraction. Since Stokes V carries information on the direction of the magnetic field along the line of sight, this indicates a potential orientation switch in the underlying magnetic field geometry. This reversal could be caused by the waves, as shown in Figure 3; we will further investigate the sign reversal in Section 3.8.

3.6. Faraday Rotation

Figure 6 (fourth row) shows maps of RMs computed between 80 and 100 GHz. The RM is defined as

$$\text{RM} = \frac{\chi_1 - \chi_2}{\lambda_1^2 - \lambda_2^2}, \quad (11)$$

where χ_ν is the EVPA computed at a specific frequency ν defined as $\chi = \frac{1}{2} \tan^{-1}(S_Q/S_U)$, and λ is the wavelength. Large RMs are visible along the jet, and in the core, we find values as large as 10^4 – 10^5 rad m^{-2} . However, the core dominates the total RM, which is expected, since the Faraday depth is larger due to higher density and lower temperatures. The relatively large value for the RM in the jet is somewhat surprising, given that the jet does not exhibit large Faraday depths. Given the small

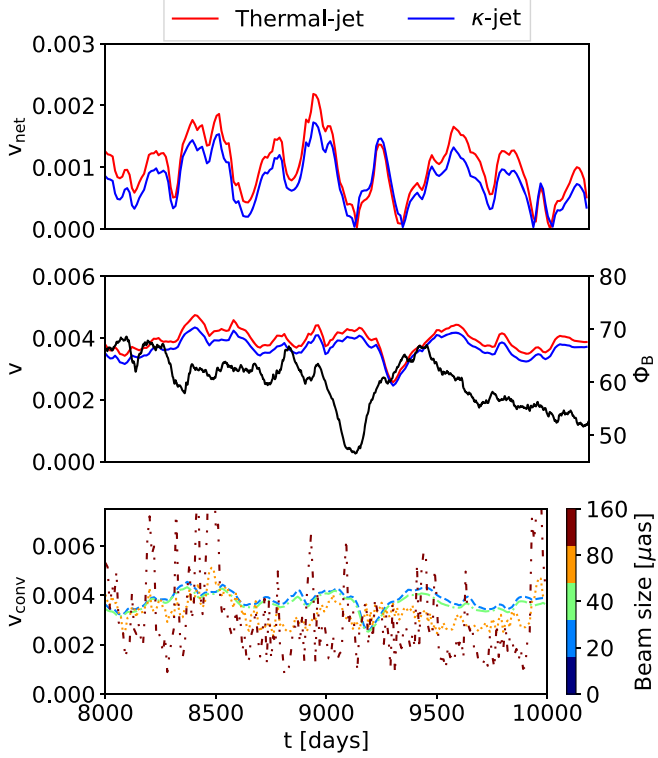


Figure 12. Identical to Figure 11 but now with the inner $30r_g$ excised from the computation of v_{net} , v , and v_{conv} . While for v_{net} , both models are similar, for v , the κ -jet model has similar CP fractions as the thermal-jet model.

Faraday depth, the change in EVPA is caused not by Faraday rotation but rather by the transverse gradients in n_e , Θ_e , and B in the emitting shear layer. These gradients result in emission at different frequencies peaking at different depths in the shear layer, which have different plasma properties; e.g., different magnetic field orientations will result in different orientations of the EVPA, giving rise to nonzero RM values.

3.7. Properties along a Ray

To test if the waves cause linear depolarization, we identified representative light rays showing high or low polarization fractions. The selected geodesics are indicated with the red, blue, and green dots in the top panel of Figure 13. We then compute the LP fraction as a function of the CKS x' coordinate, meaning smaller values of x' are closer to the spin axis. The result of this is shown in the bottom panel of Figure 13. We show the geodesics only as they approach the jet–wind surface and only show segments when the local magnetization $\sigma < 5$, meaning no radiation transfer is applied when the geodesic is inside the jet. The red ray is terminated early, meaning that for larger x' , its net polarization fraction is higher, indicating that the shear layer at that point is thinner. The blue and green rays have a larger travel path, meaning that the polarization starts to drop. In the case of the green ray, the situation is even more interesting. The line of this ray is interrupted twice, indicating that it crossed into two regions of high magnetization but then left. We interpret this as the ray crossing through a rolling wave, similar to the wave seen at $y = -100r_g$ in Figure 2. We test this by also computing the magnetization along the ray; this is also shown in the bottom panel of Figure 13 by a black line. This line crosses our magnetization threshold ($\sigma > 5$) twice. In

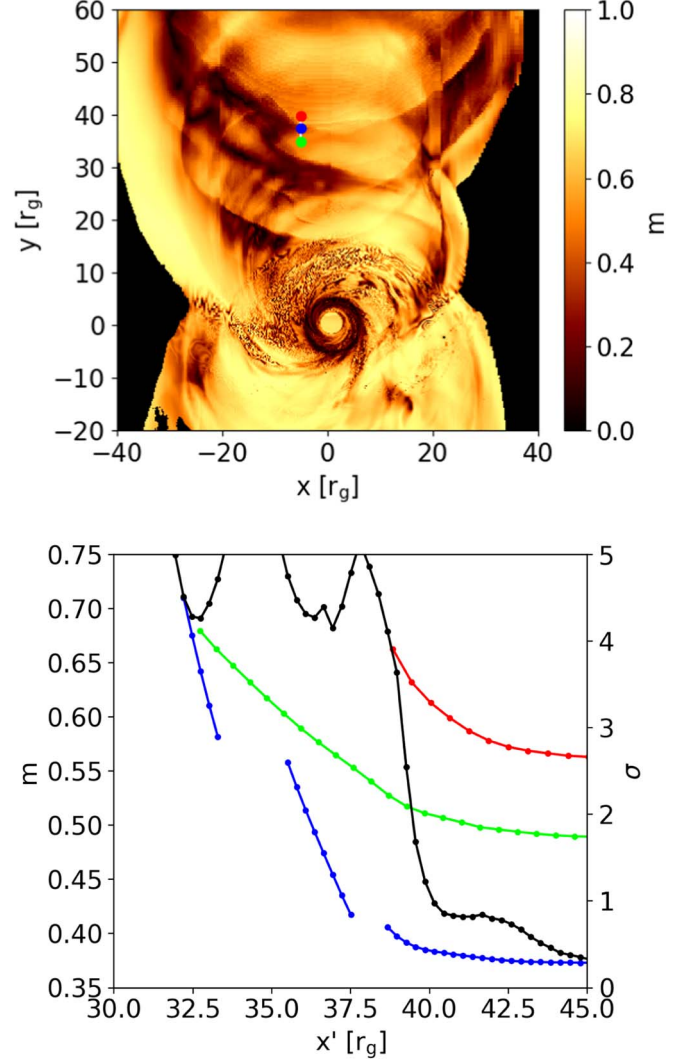


Figure 13. In the top panel, we show an LP map, m . Red, blue, and green dots indicate the pixels along which we compute the LP as a function of the geodesics x' . The dependence on x' is shown in corresponding colors in the bottom panel. The black line indicates magnetization along the pixel corresponding to the green dot (axis on the right).

general, the waves alter the thickness of the jet–wind shear layer, and their presence results in varying path lengths inside the shear layer for different rays, which affects the LP fraction.

3.8. Correlation with the Jet–Wind Shear Waves

To connect the waves in GRMHD with the structures seen in the synthetic 86 GHz images, we compute emissivity-weighted averages of the magnetization σ , the pitch angle between the wavevector and the magnetic field orientation $\cos(\theta_B)$, the electron number density n_e , and the electron temperature Θ_e via

$$\langle q \rangle = \frac{\int j_\nu q d\lambda_{\text{aff}}}{\int j_\nu d\lambda_{\text{aff}}}, \quad (12)$$

where q represents the weighted quantity; the result of this computation is shown in Figure 14. The top left panel, σ , shows that the images’ higher-intensity features also have a larger magnetization. This agrees with the waves having a larger magnetization in Figure 4. Additionally, the same

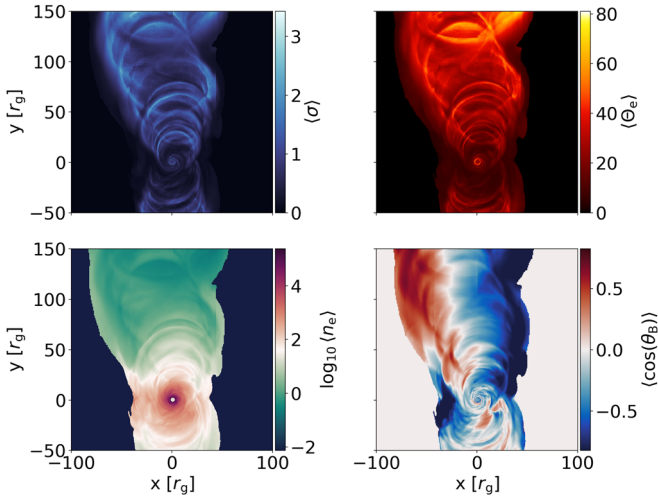


Figure 14. Emissivity-weighted averages of the magnetization σ (top left), electron temperature Θ_e (top right), electron number density n_e (bottom left), and angle between the magnetic field and wavevector $\cos(\theta_B)$ (bottom right).

patterns are visible in the higher electron temperatures (top right panel of Figure 14) and the overdensities (bottom left panel of Figure 14), also in agreement with the properties of the waves, as shown in Section 3.1.

For Stokes \mathcal{V} , we finally compare the emissivity-weighted average of $\cos(\theta_B)$ (bottom right panel of Figure 14). The overall map of $\cos(\theta_B)$, where θ_B is the angle between the wavevector and the magnetic field vector, shows the same sign as Stokes \mathcal{V} , implying that reversals in Stokes \mathcal{V} are caused by the shearing of the magnetic fields leading to reversed field orientations.

4. Discussion and Conclusion

In this Letter, we present a global GRMHD simulation in CKS coordinates in the MAD regime that shows the formation of waves along the jet–wind shear layer. We postprocess this simulation with our polarized radiative transfer code and compute polarized spectral energy distributions, time series of polarization quantities, and synthetic images at 86 GHz. We find observational signatures of the surface waves seen in the GRMHD simulation in the polarization information. As the waves propagate outward, they show up as bright features along the jet that alter the polarization signature of the jet at larger scales. As the waves alter the orientation of the magnetic field lines, the LP fraction drops due to the cancellation of subsequently rotated Stokes vectors.

During magnetic flux eruptions, we find an inverse relation between Φ_B and the LP fraction, meaning that as Φ_B drops, the LP fraction increases. We see the opposite for the CP, where the fraction decreases as Φ_B decreases. Both effects can be explained by the flux eruption ejecting the disk near the horizon; as the strong poloidal field arrests parts of the disk, the density drops, and the disk becomes more optically and Faraday thin, leading to lower Faraday rotation and conversion. This results in a decrease in CP and an increased LP fraction.

At the largest magnetic flux eruption in our simulation, we find that the unresolved Stokes \mathcal{Q} and \mathcal{U} at 3 mm show a clockwise loop in a $\mathcal{Q} - \mathcal{U}$ diagram with a polarization excess of $m_{\text{net}} \sim 0.06$. Loops like this were previously identified in the case of our galactic supermassive black hole SgrA*, either observationally (Marrone et al. 2008; Wielgus et al. 2022; The

GRAVITY Collaboration et al. 2023) or in theoretical works (e.g., Vos et al. 2022; Najafi-Ziyazi et al. 2023). A key difference is that the timescales in the case of M87 are longer, which puts the period of our loop at ~ 3 months, compared to ~ 1 hr in the case of SgrA*.

Our model recovers resolved polarization fractions that are too high compared to the ones measured by Hada et al. (2016). However, when convolved with a more realistic telescope beam, we show that the LP fraction substantially drops, since \mathcal{Q} and \mathcal{U} are averaged out due to patches within the beam having opposing signs. We find consistent RMs without invoking an external Faraday screen, and we recover the observed spectral shape from radio to optical frequencies (EHT MWL Science Working Group et al. 2021). Although we limit ourselves to M87, our results generally apply to other LLAGNs reaching the MAD state, since the waves result from the underlying flow geometry and flux eruptions typical for such systems. We expect these polarization signatures to be independent of black hole masses and accretion rates.

In the literature, studies of wave instability at jet–wind shear layers are typically limited to analytical studies, e.g., linear analysis (Ferrari et al. 1978; Sobacchi & Lyubarsky 2018; Chow et al. 2023) or with numerical MHD/particle-in-cell studies of local idealized setups (Hardee et al. 2007; Perucho et al. 2010; Sironi et al. 2021). The overall conclusions of these works are that jets, if in the right conditions, can be prone to the excitation of waves due to linear instability, e.g., Kelvin–Helmholtz waves. These waves are asymmetric, meaning they have different plasma properties on either side of the shear layer. Previous work by Sironi et al. (2021) showed that particles can be accelerated to high energies in mildly relativistic, magnetized asymmetric shear flows. However, evidence of wave instabilities in global simulations is sparse and often underresolved in 3D simulations due to the restrictions on the large-scale resolution in spherical coordinates; see Chatterjee et al. (2019) and Wong et al. (2021). Observationally, some evidence for wavelike perturbations at large distances from the central engine is found by, e.g., Perucho & Lobanov (2007), Pasetto et al. (2021), and Issaoun et al. (2022).

In this work, we did not perform a rigorous linear analysis to determine if the waves could be grown from linear scales and what instability is driving them. Visually, the jet is initially stable and shows no waves, while when the system reaches the MAD state and the first flux eruptions occur, waves travel outward along the jet–wind boundary. Therefore, the waves we see are more likely to grow by forced oscillations of the jet base due to accretion variability and ejecta from magnetic flux eruptions. The waves are already nonlinear within a few gravitational radii, which would require short linear growth times. A more likely scenario is that the jet base’s variability efficiently drives the waves’ growth and becomes nonlinear at larger scales. A study of the conditions under which these waves are growing by either applying linear analysis (Chow et al. 2023) to local conditions extracted from our simulation or performing local idealized simulations will be done in future works.

Compared to previous global simulations of LLAGN jets, our simulations stand out due to the Cartesian nature of the grid, allowing us to resolve the jet to larger distances compared to more standard simulations with spherical grids as used in, e.g., Event Horizon Telescope Collaboration et al. (2019b).

This higher resolution enables us to follow the perturbations at the jet base to larger scales. However, the waves we see in our simulations are not a result of our choice of coordinates and can be found in spherical simulations if run at sufficiently high resolution (Ripperda et al. 2022), as shown in Appendix A.

The evidence we find for the shear layer waves in our simulation may have implications for particle energization. The waves could introduce a source of turbulence or reconnection in the shear layer (Sironi et al. 2021). These processes could lead to electron acceleration, resulting in nonthermal emission that could explain the edge brightening of AGN jets. Additionally, reconnection induced by the waves could drive injection of high-energy ions originating from the disk into shear-driven acceleration, potentially producing ultrahigh-energy cosmic rays; see, e.g., Caprioli (2015), Rieger (2019), and Mbarek & Caprioli (2021).

In this work, we discover a correlation between jet–wind surface waves and polarized emission properties. We find evidence that the substructure in the jet, in the form of waves, imprints itself on the Stokes I and LP maps. We identify ridges and alternating low and high LP fractions as telltale signatures of these waves. Although currently below the achievable resolution of VLBI arrays, this effect might be resolvable by next-generation arrays, such as the ng-EHT (Issaoun et al. 2023; Ricarte et al. 2023). If the ng-EHT operates at 86 GHz, it will achieve a resolution of $\sim 60 \mu\text{as}$, or $20r_g$ scaled to M87, which would be sufficient for resolving the features we find in this study.

Acknowledgments

J.D. is supported by a Joint Columbia University and Flatiron Institute Postdoctoral Fellowship. Research at the Flatiron Institute is supported by the Simons Foundation. B.R. is supported by the Natural Sciences & Engineering Research Council of Canada (NSERC). L.S. acknowledges support from the Cottrell Scholars Award and DoE Early Career Award DE-SC0023015. L.S. and J.D. acknowledge support from NSF AST-2108201. A.P. acknowledges support by NASA ATP grant 80NSSC22K1054. H.O. was supported by a Virtual Institute of Accretion (VIA) postdoctoral fellowship from the Netherlands Research School for Astronomy (NOVA). K.C. acknowledges support from grants from the Gordon and Betty Moore Foundation and the John Templeton Foundation to the Black Hole Initiative at Harvard University and from NSF award OISE-1743747. This work was supported by a grant from the Simons Foundation (MP-SCMPS-00001470) to L.S. and A.P. and facilitated by the Multimessenger Plasma Physics Center (MPPC), NSF grants PHY-2206609 and PHY-2206610.

The computational resources and services used in this work were partially provided by facilities supported by the Scientific Computing Core at the Flatiron Institute, a division of the Simons

Foundation, and by the VSC (Flemish Supercomputer Center), funded by the Research Foundation Flanders (FWO) and the Flemish Government department EWI. This research was enabled by support provided by grant No. NSF PHY-1125915 along with INCITE program award PHY129 using resources from the Oak Ridge Leadership Computing Facility, Summit, which is a US Department of Energy Office of Science User Facility supported under contract DE-AC05-00OR22725, as well as Calcul Quebec (<http://calculquebec.ca>) and Compute Canada (<http://compute-canada.ca>). The computational resources and services used in this work were partially provided by facilities supported by the Scientific Computing Core at the Flatiron Institute, a division of the Simons Foundation. This research is part of the Frontera (Stanzione et al. 2020) computing project at the Texas Advanced Computing Center (LRAC-AST20008). Frontera is made possible by National Science Foundation award OAC-1818253.

Software: python (Oliphant 2007; Millman & Aivazis 2011), scipy (Jones et al. 2001), numpy (van der Walt et al. 2011), matplotlib (Hunter 2007), RAPTOR (Bronzwaer et al. 2018, 2020), BHAC (Porth et al. 2017; Olivares et al. 2019).

Appendix A GRMHD Coordinate Comparison

To assess if the waves shown in our simulation are a robust feature, we cross-compared our CKS simulation with a set of modified Kerr–Schild (MKS) simulations on a spherical coordinate basis at varying resolutions run with the HAMR code (Liska et al. 2022) and presented in Ripperda et al. (2022). All simulations are initialized with identical initial conditions to our CKS simulation. In Table 1, we show the cells in the θ and ϕ directions on the horizon and the number of cells per jet radius. We use a jet radius of approximately $50r_g$, where we find typical wave structures in our simulations.

We cross compared our CKS simulations with the four spherical simulations at different resolutions by computing various quantities close to the event horizon. The result of this is shown in Figure 15. We do this by comparing the mass accretion rate computed at $r = 5r_g$ (top panel) as well as the magnetic flux threading the horizon (bottom panel), and the MAD parameter $\phi_{\text{mad}} = \Phi_B/\sqrt{m}$, for all four resolutions. All simulations reach, on average, similar values of all three quantities and obtain a MAD state at $t \sim 3000\text{--}4000r_g/c$. During the remainder of the simulations, multiple flux eruptions are visible in Φ_B that look similar among all simulations, e.g., similar slopes when Φ_B drops and similar fractional decreases. The horizon-integrated quantities, therefore, indicate a convergence of the global dynamics typical for a MAD accretion flow.

Table 1
Summary of the Number of Cells, Horizon Resolution, and Jet Resolution at $r = 50r_g$ for Our BHAC and HAMR Models

Model	$N_r \times N_\theta \times N_\phi$	Cells on Horizon	Cells per Jet Radius at $50r_g$
BHAC CKS	...	54×107	150
HAMR MKS low	$288 \times 128 \times 128$	128×128	40
HAMR MKS standard	$580 \times 288 \times 256$	288×256	91
HAMR MKS high	$2240 \times 1056 \times 1024$	1056×1024	332
HAMR MKS extreme	$5376 \times 2304 \times 2304$	2304×2304	733

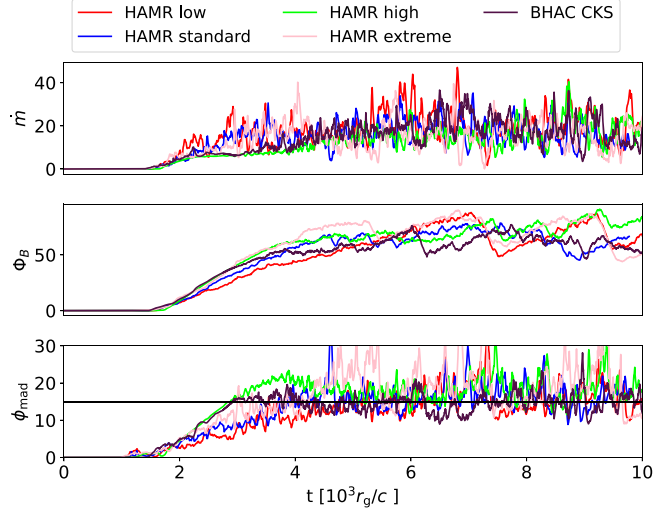


Figure 15. Comparison between BHAC CKS and HAMR MKS for varying resolutions. Shown are the mass accretion rate \dot{m} (top), magnetic flux Φ_B (middle), and MAD parameter ϕ_{mad} (bottom).

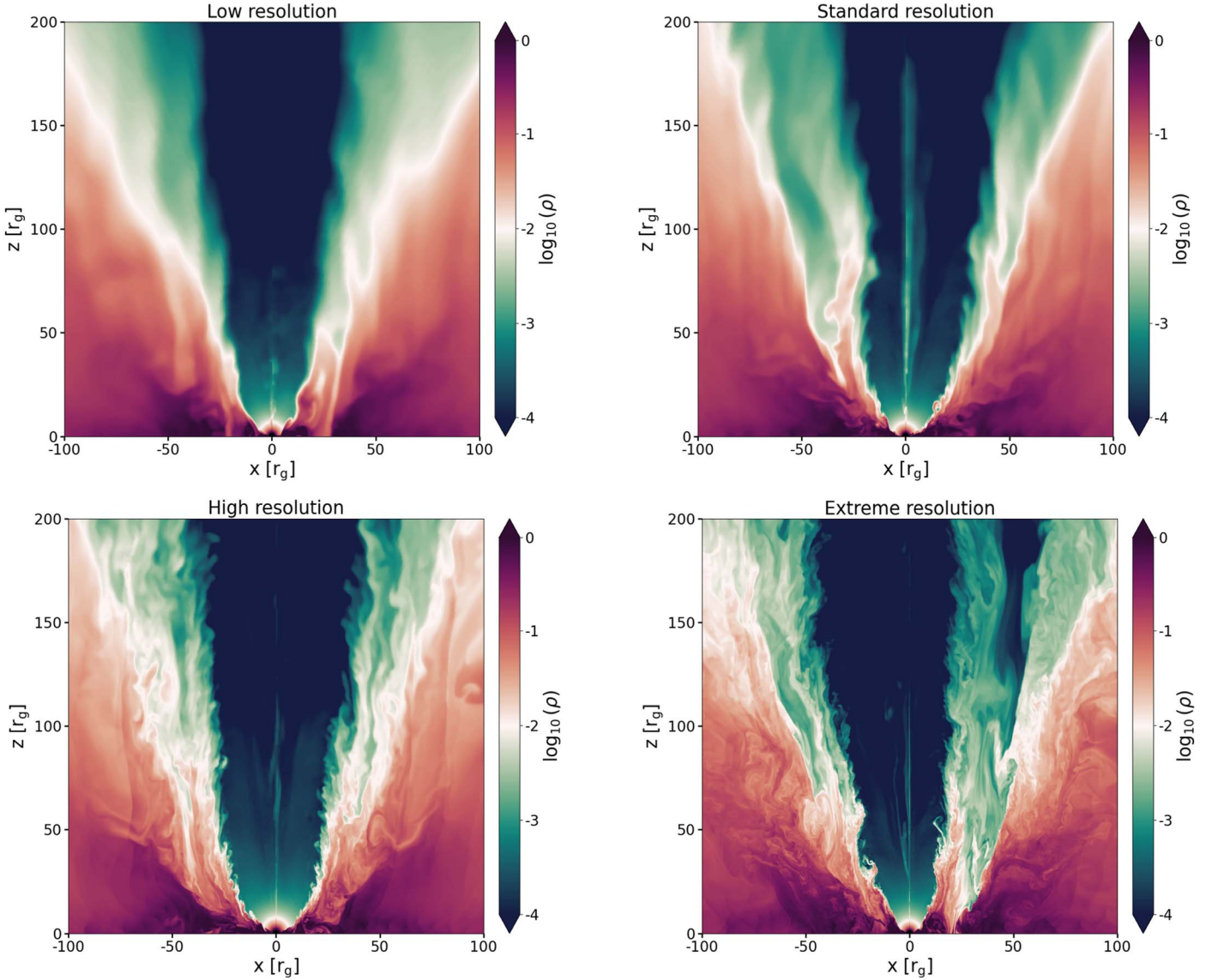


Figure 16. Simulation snapshots at $t = 10,000 r_g/c$ for the four HAMR MKS models at varying resolution. Shown are slices along the $x-z$ plane of the logarithm of density. As the resolution increases from left to right and top to bottom, the simulations show a more extended substructure in the form of waves along the jet-wind interface, where the two lowest resolutions are more diffuse than the highest resolutions.

Finally, we show slices along the x - z axis of the HAMR simulations in Figure 16. The jet of four simulations in spherical coordinates shows similar opening angles as our Cartesian simulation in Figure 1. As the resolution increases, we see more and more substructure in the form of waves along the jet-wind interface, whereas the two lowest resolutions are more diffuse. Compared to Figure 2, our simulation falls somewhere between the standard and high-resolution runs, which is unsurprising given that the jet resolutions of our CKS run are also between these two spherical runs. However, due to the larger horizon cells, the CKS simulation has a substantially lower computational cost, $\approx 500,000$ CPU hr, similar to the low-resolution case runtimes. Additionally, we resort to postprocessing the BHAC CKS simulation over the higher-resolution HAMR simulation for a more practical reason: to date, there is no radiation transfer code that can read in and process the adaptive mesh refinement (AMR) based grid structure of HAMR. Additionally, the extreme resolutions achieved by HAMR would result in a large memory demand as well. We aim to develop an extended, more efficient version of RAPTOR that is fully coupled to the HAMR data format that will be capable of ray-tracing the full extreme-resolution simulation in the future.

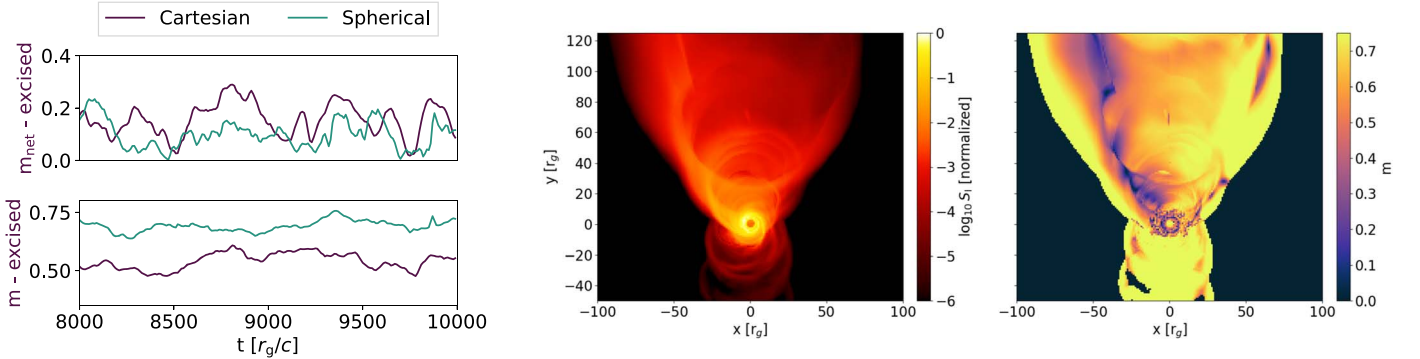


Figure 17. Left: LP fraction as a function of time for both the Cartesian and spherical simulations. Both panels exclude the core emission within $30r_g$ of the image origin. Top: net LP fraction m_{net} , showing similar values. Bottom: resolved LP fraction m , showing a clear factor of 1.5 difference. Middle: Stokes I map of the spherical simulation, which shows limited substructure. Right: LP fraction map of the spherical simulation. A limited amount of structure is visible compared to the Cartesian case and shows a substantially higher LP fraction, $m \sim 0.75$ vs. $m \sim 0.5$.

Appendix B Comparison to Low-resolution Spherical Kerr–Schild

We cross-compared our CKS MAD simulation with a low-resolution spherical MKS simulation to further strengthen our conclusions. The MKS simulation has a base resolution of [96, 48, 48] in r , θ , ϕ , and one additional level of AMR. The simulation was run up to $t = 10,000r_g/c$ with BHAC. Due to the low resolution in this simulation’s jet region, no waves are present along the jet-wind surface. Note that due to the low resolution, the physical solution of this simulation is far from resolved and, therefore, in an unrealistically low regime of Reynolds number. We only use it here to compare a laminar flow to a flow where the jet-wind surface shows wave instabilities. We ray-trace the spherical simulation over the final $2000r_g/c$ with the same model and camera parameters as the κ -jet model presented in the main text. Comparing the resolved LP fraction with the higher-resolution Cartesian case shows a substantially higher fraction, namely, at $m \sim 0.7$, compared to $m \sim 0.5$; see Figure 17 (left panel). The synthetic LP image, shown in Figure 17 (right panel), also does not show any wavelike substructure, which is in stark contrast to the Cartesian case. This comparison, therefore, further confirms our hypothesis that the jet-wind shear layer waves, which are only captured with sufficiently high resolution, lead to the drop in LP fraction.

ORCID iDs

J. Davelaar <https://orcid.org/0000-0002-2685-2434>
 B. Ripperda <https://orcid.org/0000-0002-7301-3908>
 L. Sironi <https://orcid.org/0000-0002-1227-2754>
 A. A. Philippov <https://orcid.org/0000-0001-7801-0362>
 H. Olivares <https://orcid.org/0000-0001-6833-7580>
 O. Porth <https://orcid.org/0000-0002-4584-2557>
 T. Bronzwaer <https://orcid.org/0000-0003-1151-3971>
 K. Chatterjee <https://orcid.org/0000-0002-2825-3590>

References

Bronzwaer, T., Davelaar, J., Younsi, Z., et al. 2018, *A&A*, **613**, A2
 Bronzwaer, T., Younsi, Z., Davelaar, J., & Falcke, H. 2020, *A&A*, **641**, A126
 Caprioli, D. 2015, *ApJL*, **811**, L38
 Chael, A., Narayan, R., & Johnson, M. D. 2019, *MNRAS*, **486**, 2873
 Chatterjee, K., Liska, M., Tchekhovskoy, A., & Markoff, S. B. 2019, *MNRAS*, **490**, 2200
 Chow, A., Davelaar, J., Rowan, M. E., & Sironi, L. 2023, *ApJL*, **951**, L23
 Cruz-Osorio, A., Fromm, C. M., Mizuno, Y., et al. 2022, *NatAs*, **6**, 103
 Davelaar, J., & Haiman, Z. 2022, *PhRvD*, **105**, 103010
 Davelaar, J., Mościbrodzka, M., Bronzwaer, T., & Falcke, H. 2018, *A&A*, **612**, 16
 Davelaar, J., Olivares, H., Porth, O., et al. 2019, *A&A*, **632**, 16
 Dexter, J. 2016, *MNRAS*, **462**, 115
 Dexter, J., McKinney, J. C., & Agol, E. 2012, *MNRAS*, **421**, 1517
 Dexter, J., Tchekhovskoy, A., Jiménez-Rosales, A., et al. 2020, *MNRAS*, **497**, 4999
 Event Horizon Telescope Collaboration, Akiyama, K., Alberdi, A., et al. 2019a, *ApJL*, **875**, L1
 Event Horizon Telescope Collaboration, Akiyama, K., Alberdi, A., et al. 2019b, *ApJL*, **875**, L5
 Event Horizon Telescope Collaboration, Akiyama, K., Alberdi, A., et al. 2022, *ApJL*, **930**, L16
 Event Horizon Telescope Collaboration, Akiyama, K., Algaba, J. C., et al. 2021, *ApJL*, **910**, L12
 EHT MWL Science Working Group, Algaba, J. C., Anczarski, J., et al. 2021, *ApJL*, **911**, L11
 Falcke, H., Melia, F., & Agol, E. 2000, *ApJL*, **528**, L13
 Ferrari, A., Trussoni, E., & Zaninetti, L. 1978, *A&A*, **64**, 43
 Fishbone, L. G., & Moncrief, V. 1976, *ApJ*, **207**, 962
 Fromm, C. M., Cruz-Osorio, A., Mizuno, Y., et al. 2022, *A&A*, **660**, A107
 Giovannini, G., Savolainen, T., Orienti, M., et al. 2018, *NatAs*, **2**, 472
 Hada, K., Kino, M., Doi, A., et al. 2016, *ApJ*, **817**, 131
 Hakobyan, H., Ripperda, B., & Philippov, A. A. 2023, *ApJL*, **943**, L29
 Hardee, P., Mizuno, Y., & Nishikawa, K.-I. 2007, *Ap&SS*, **311**, 281
 Hunter, J. D. 2007, *CSE*, **9**, 90
 Igumenshchev, I. V., Narayan, R., & Abramowicz, M. A. 2003, *ApJ*, **592**, 1042
 Issaoun, S., Pesce, D. W., Roelofs, F., et al. 2023, *Galax*, **11**, 28
 Issaoun, S., Wielgus, M., Jorstad, S., et al. 2022, *ApJ*, **934**, 145
 Janssen, M., Falcke, H., Kadler, M., et al. 2021, *NatAs*, **5**, 1017
 Jones, E., Oliphant, T., Peterson, P., et al. 2001, SciPy: Open Source Scientific Tools for Python
 Kim, J.-Y., Krichbaum, T. P., Lu, R.-S., et al. 2018, *A&A*, **616**, 13
 Liska, M. T. P., Chatterjee, K., Issa, D., et al. 2022, *ApJS*, **263**, 26
 Lu, R.-S., Asada, K., Krichbaum, T. P., et al. 2023, *Natur*, **616**, 686
 Luminet, J. P. 1979, *A&A*, **75**, 228
 Marrone, D. P., Baganoff, F. K., Morris, M. R., et al. 2008, *ApJ*, **682**, 373
 Marszewski, A., Prather, B. S., Joshi, A. V., Pandya, A., & Gammie, C. F. 2021, *ApJ*, **921**, 17
 Mbarek, R., & Caprioli, D. 2021, *ApJ*, **921**, 85
 Millman, K. J., & Aivazis, M. 2011, *CSE*, **13**, 9
 Mościbrodzka, M., Dexter, J., Davelaar, J., & Falcke, H. 2017, *MNRAS*, **468**, 2214
 Mościbrodzka, M., Falcke, H., & Shiokawa, H. 2016, *A&A*, **586**, A38
 Najafi-Ziyazi, M., Davelaar, J., Mizuno, Y., & Porth, O. 2023, arXiv:2308.16740
 Narayan, R., Igumenshchev, I. V., & Abramowicz, M. A. 2003, *PASJ*, **55**, L69
 Narayan, R., Palumbo, D. C. M., Johnson, M. D., et al. 2021, *ApJ*, **912**, 35
 Oliphant, T. E. 2007, *CSE*, **9**, 10
 Olivares, H., Porth, O., Davelaar, J., et al. 2019, *A&A*, **629**, 21
 Pandya, A., Zhang, Z., Chandra, M., & Gammie, C. F. 2016, *ApJ*, **822**, 34
 Park, J., Hada, K., Kino, M., et al. 2019, *ApJ*, **871**, 257
 Pasetto, A., Carrasco-González, C., Gómez, J. L., et al. 2021, *ApJL*, **923**, L5
 Perucho, M., & Lobanov, A. P. 2007, *A&A*, **469**, L23
 Perucho, M., Martí, J. M., Cela, J. M., et al. 2010, *A&A*, **519**, A41
 Porth, O., Mizuno, Y., Younsi, Z., & Fromm, C. M. 2021, *MNRAS*, **502**, 2023
 Porth, O., Olivares, H., Mizuno, Y., et al. 2017, *ComAC*, **4**, 1
 Prieto, M. A., Fernández-Ontiveros, J. A., Markoff, S., Espada, D., & González-Martín, O. 2016, *MNRAS*, **457**, 3801
 Ricarte, A., Johnson, M. D., Kovalev, Y. Y., Palumbo, D. C. M., & Emami, R. 2023, *Galax*, **11**, 5
 Rieger, F. M. 2019, *Galax*, **7**, 78
 Ripperda, B., Bacchini, F., & Philippov, A. A. 2020, *ApJ*, **900**, 100
 Ripperda, B., Liska, M., Chatterjee, K., et al. 2022, *ApJL*, **924**, L32
 Rybicki, G. B., & Lightman, A. P. 1979, *Radiative Processes in Astrophysics* (Wiley (New York: Wiley))
 Shcherbakov, R. V. 2008, *ApJ*, **688**, 695
 Sironi, L., Rowan, M. E., & Narayan, R. 2021, *ApJL*, **907**, L44
 Sironi, L., & Spitkovsky, A. 2014, *ApJL*, **783**, L21
 Sobacchi, E., & Lyubarsky, Y. E. 2018, *MNRAS*, **473**, 2813
 Stanzione, D., West, J., Evans, R. T., et al. 2020, *Practice and Experience in Advanced Research Computing, PEARC '20* (New York: Association for Computing Machinery), 106
 Tchekhovskoy, A., Narayan, R., & McKinney, J. C. 2011, *MNRAS*, **418**, L79
 The GRAVITY Collaboration, Abuter, R., Aimar, N., et al. 2023, *A&A*, **677**, L10
 van der Walt, S., Colbert, S. C., & Varoquaux, G. 2011, *CSE*, **13**, 22
 Vos, J., Mościbrodzka, M. A., & Wielgus, M. 2022, *A&A*, **668**, A185
 Walker, R. C., Hardee, P. E., Davies, F. B., Ly, C., & Junor, W. 2018, *ApJ*, **855**, 128
 Wielgus, M., Mościbrodzka, M., Vos, J., et al. 2022, *A&A*, **665**, L6
 Wong, G. N., Du, Y., Prather, B. S., & Gammie, C. F. 2021, *ApJ*, **914**, 55
 Xiao, F. 2006, *PPCF*, **48**, 203
 Zavala, R. T., & Taylor, G. B. 2003, *ApJ*, **589**, 126
 Zhdankin, V., Ripperda, B., & Philippov, A. A. 2023, *PhRvR*, **5**, 043023